Environmental Science Nano

Coupled Morphological and Structural Evolution of **δ-MnO2** to **α-MnO2** through Multistage Oriented Assembly Processes: the Role of Mn(III)

Journal:	*Environmental Science: Nano*
Manuscript ID	EN-ART-09-2019-001000.R1
Article Type:	Paper

Environmental Significant

δ-MnO_2 and α-MnO_2 are widespread near and on the earth's surface and play an important role in elemental cycles and pollutant dynamics. These behaviors are closely related to structure and morphology of the minerals. Although documented in the literature, α-MnO_2 nanorods crystal growth processes and the relationship between the structural transformation and morphological evolution are not clearly understood. In this study, the transformation of the layer-based δ-MnO_2 to tunnel-based α-MnO_2 occurs via a multistage OA process. The disordered structure produced by δ-MnO_2 nanoflakes OA process facilitates the reduction of Mn(IV) in the layer to Mn(III) and Mn(III) migrates out to the interlayer. Interlayer Mn(III) promotes the face-to-face OA of adjacent nanoribbons to form a nanorod and to form a 2 × 2 α-MnO_2 tunnel structure as tunnel "walls". These findings provide insights into not only the transformation mechanisms of the layer-based to the tunnel-based nanoparticles in the environment but also efficient and controlled synthesis of environmentally friendly materials

Coupled Morphological and Structural Evolution of δ-MnO_2 to α-MnO_2 through Multistage Oriented Assembly Processes: the Role of Mn(III)

Xinran Liang,[a, b] Jeffrey E. Post,[c] Bruno Lanson,[d] Xiaoming Wang,[a] Mengqiang Zhu,[e] Fan Liu,[a] Wenfeng Tan,[a] Xionghan Feng,[a*] Guomin Zhu,[b] Xin Zhang,[b] James. J. De Yoreo[b]

a Key Laboratory of Arable Land Conservation (Middle and Lower Reaches of Yangtse River), Ministry of Agriculture, College of Resources and Environment, Huazhong Agricultural University, Wuhan 430070, China

b Physical Sciences Division, Pacific Northwest National Laboratory, Richland, WA 99352 United States

c Department of Mineral Sciences, Smithsonian Institution, Washington, DC 20013, USA

d University of Grenoble Alpes, CNRS, ISTerre, F-38000 Grenoble, France

e Department of Ecosystem Science and Management, University of Wyoming, Laramie, WY, 82071, United States.

ABSTRACT: α-MnO_2 is a typical tunneled Mn oxide (TMOs) which frequently associated with δ-MnO_2 in the environment exhibits strong adsorption and oxidation activity. The morphology of α-MnO_2 which controlled by oriented attachment process (OA) is one of the key factors affecting its reactivity. However, the detailed crystal growth process and coupling between morphology and structure of α-MnO_2 during OA processes remain poorly understood. We propose that the transformation of the layer-based δ-MnO_2 to tunnel-based α-MnO_2 occurs via a multistage OA process. In the initial stage, the produced δ-MnO_2 nanoflakes are found to spontaneously self-assemble into a nanoribbon with a large number of lattice defects via edge-to-edge OA. The presence of lattice defects promotes the generation of oxygen vacancies, and the Mn(IV) ions in the [MnO_6] octahedral layers of δ-MnO_2 is reduced to Mn(III)/Mn(II). The reduced ions subsequently migrate from the [MnO_6] octahedral layers to the interlayers during this process. Driven by hydrogen bonding between hydroxide which acts in coordination with the interlayer Mn(III)/Mn(II) and oxygen atoms coordination with adjacent nanoribbons attach to each other and form primary nanorods through a face-to-face OA mechanism along the *c*-axis. Concomitantly, the bonding of [Mn(III)O_6] octahedra in the interlayer of the nanoribbons with adjacent [MnO_6] octahedral layers lead to the fabrication of a new α-MnO_2 tunnel structure from the original δ-MnO_2. These findings provide insights into both the transformation mechanisms of the layer-based to the tunnel-based nanoparticles and methods for efficient and controlled synthesis of nanomaterials.

INTRODUCTION

Oriented attachment (OA) is a nonclassical mechanism of crystal growth, and proceeds by repeated attachment events of crystalline particles on specific crystal faces that are lattice-matched with true crystallographic alignment.[1] The growth of many crystalline substances, including engineered nanomaterials and the natural nanoparticles, has been reported to occur via the OA mechanism.[2] These properties of nanoparticles are closely related to their morphologies and structures. The OA process only leads to the morphological evolution, as indicated in previous reports, while the processes of structural changes associated with morphological evolutions have been explored to a lesser extent.[1-2] Revealing the coupling relationship between morphological evolutions and structural changes during the OA process is not only important for controlling the synthetic materials but also for proving the novel idea for the study of crystal growth.[3]

Recent studies have reported that poor crystallinity layer manganese oxide (LMO) nanoparticles assemble as LMO nanoflowers and tunneled manganese oxide (TMO) nanorods via the OA mechanism.[4-8] LMO-to-TMO reaction mechanisms have been extensively investigated because LMOs association with TMOs occur frequently in the environment.[5, 8-10] In addition, LMOs and TMOs have also been extensively applied as materials in catalysis, ion exchange, energy storage, and octahedral molecular sieves.[9–10] There are some detailed studies on the structural evolution and a few studies on the morphological evolution during LMO-to-TMO reactions.[8, 11] The two separate studies on the structural and morphological evolution indicate there are some difficulties in understanding their coupling relationship and the reaction mechanism of the LMO-to-TMO process in the environment.

In natural environment, cryptomelane (α-MnO_2) represents an important family of TMOs with 2 × 2 and 1 × 1 (intergrowth little 2 × 3, 2 × 4 and "T" junction structure, etc.) tunnel structures, which are formed when double chains of edge-sharing [MnO_6] octahedra share corners with neighboring chains (Figure S1A).[12, 13] The larger tunnels are generally stabilized by K^+, Ba^+, and Na^+.[14] Cryptomelane is the major manganese oxide in the supergene oxidation zones of Mn-bearing crusts and manganese deposits and lateritic weathered profiles.[15-176] The unique physicochemical properties of α-MnO_2 have provided

a wide range of potential applications in removing the environment pollutions.[18–20] These applications are considerably affected by the structure and morphology of α-MnO_2.[20]

δ-MnO_2 (Figure S1B) is the most common LMO in the environment with strong adsorption and oxidation activity frequently associated with α-MnO_2.[11] It was proposed that the formation and migration of Mn(III) occurred while δ-MnO_2 transform to α-MnO_2.[21] Yuan et al, also reported that the transforming process of well crystallinity buserite to todorokite (2 × 3 tunnel structure) through Mn(III) migration by the combination of morphology, structure and theoretical calculation.[22] Additionally, a detailed OA process based on the formation of long α-MnO_2 nanorods from α-MnO_2 primary nanorods was also reported.[20, 23–24] However, the formation process of the primary α-MnO_2 nanorods from poor crystallinity δ-MnO_2 nanoparticles is still unknown due to too fast or slow conversion rate under different reaction conditions which is detrimental to the capture of the transition state.[12, 13] In addition, it is unclear how the new tunnel structure formation corresponds with the morphological evolution by the OA process. A basic knowledge of the morphological evolution across the entire synthetic process and the relationship with the structural transformation are also critical for the α-MnO_2 material synthesis in various applications, and the understanding of the minerology and behavior of different type of MnO_2 minerals in nature.

In this study, Na^+/K^+-stabilized α-MnO_2 which similar to environment cryptomelane nanorods were synthesized by co-precipitation of Na/$KMnO_4$ with $MnSO_4$. The dynamic process of the formation of the Na^+-stabilized α-MnO_2 nanorods was carefully explored. Given that the Na^+-stabilized α-MnO_2 forms at a slower rate compared to that of K^+, as shown in previous experiments, it provides a more suitable system for the investigation of the process of α-MnO_2 formation.[14] During the synthesis, intermediate products were sampled and quenched in liquid N_2 at different time intervals to stop crystal growth and to capture in situ morphologies and structures. These intermediate samples were characterized by pair distribution function (PDF), and X-ray photoelectron spectroscopy (XPS), to illustrate the structural changes at the atomic level. Meanwhile, morphological changes during the formation process were revealed with the use of high-resolution transmission electron microscopy (HRTEM) and field-emission scanning electron microscopy

(FESEM). Possible mechanisms for the observed coupling relationship between morphological and structural evolutions are proposed.

EXPERIMENTAL SECTION

Synthesis of different types of cations of *α*-MnO_2. In a typical experiment, 8.45 g $MnSO_4 \cdot H_2O$ (0.5 M) in 100 mL of acetic acid (2 M) and 80 mL aqueous solution of $AMnO_4$ (0.4375 M, A= K or Na) were mixed together under vigorous stirring at 60 ℃. This suspension was heated to 100 ℃ for 20 min and was then cool to 80 ℃ in open air. After cooling to 80 ℃, the suspension was frozen by liquid nitrogen and washed until the conductivity of the supernatant was less than 20.0 μS cm^{-1}, the suspension was then freeze-dried.[25]

After the two solutions were mixed and the suspension was heated to 100 ℃, 10 mL of the suspension was extracted into a 50 mL centrifuge tube filled with 20 mL of liquid nitrogen at 0, 2, 4, 6, 8, 10, 14, 16 and 20 min. The extracted samples were centrifuged at 12,000 rpm for 8 min and the precipitates were washed with 50 mL of DDW multiple times until the conductivity of the supernatant was less than 20.0 μS cm^{-1}.The precipitates were then freeze-dried for characterization. Samples were labelled AMix, A100-X and A80, where X is the heating time at 100 ℃ and A is the type of cation.

Powder X-ray diffraction. The XRD patterns were collected from the dried powders using a cavity mount on a Bruker D8 Advance diffractometer equipped with a LynxEye detector, using Ni-filtered Cu Kα radiation (λ = 0.15418 nm). The diffractometer was operated at a tube voltage of 40 kV and a current of 40 mA, with a scanning rate of 1°/min and a step size of 0.02°.

Elemental analysis and Mn AOS. The chemical composition of the samples was determined by dissolving ~ 0.1 g of each powder sample in 25 mL of 0.25 mol/L $NH_2OH \cdot HCl$. The concentrations of dissolved Mn and K were measured using inductively coupled plasma (ICP) and flame spectrometry, respectively. Mn average oxidation state (AOS) was measured by a back-titration method using a $KMnO_4$ standard solution.[26]

X-ray photoelectron spectroscopy. X-ray photoelectron spectra were collected using a VG Multilab2000 X-ray photoelectron spectrometer with an Al K X-ray source (1486 eV) and a base pressure of 3×10^{-9} Torr in the analytical chamber. The scans were recorded using the large area mode. The survey scans were collected using a fixed pass

energy of 100 eV and an energy step size of 1.0 eV, whereas the narrow scans have a pass energy of 25 eV and an energy step size of 0.1 eV. The charge effect was corrected by adjusting the binding energy (BE) of C (1s) to 284.62 eV. The spectra were analyzed using the Avantage software. The Shirley-type background was subtracted before deconvolution and fitting. The parameters used by Nesbitt et al for the multiple peaks of Mn ($2p_{3/2}$) and Mn3s for spectra fitting were adopted.[27] A 20:80 ratio of the Lorentzian: Gaussian mix-sum function was used for all the fittings.

Transmission electron microscopy. The particle size and morphology of the samples were further examined on a JEM-2100F transmission electron microscope and FEI Titan 80/300 environmental transmission electron microscopy. Prior to observation, samples were embedded in epoxy resin, left to polymerize for 48 h in the dark and cut with an ultramicrotome (Leica EM UC6) equipped with a diamond knife. The ~50nm thick sections were picked up on lacey carbon films loaded on Cu grids. In addition to assess possible preparation-induced artefacts (use of an ultramicrotome), all sample were prepared according to the above described protocol, filtered and re-suspended in ethanol. A drop of the obtained suspension was deposited on a copper microscope grid covered with perforated carbon.

Atomic Force Microscopy. All of the images were recorded in air using tapping mode on a MultiMode VIII AFM (Bruker, CA). Rfespa-190 probes (Bruker, CA) were used in the experiment. The raw data were further analyzed using NanoScope Analysis v 1.50 offline software (Bruker, CA).

Field-emission scanning electron microscopy. Detailed three-dimensional morphologies of particles were observed by using a field emission scanning electron microscope (SU8010, Hitachi) with a maximum resolution of 1 nm. For high-resolution SEM, the microscope was operated at 15 kV and the working distance was 0.5-30 mm; an in-lens secondary electron detector was used. Prior to SEM analysis, each sample was gold-coated.

High-energy X-ray total scattering. Synchrotron-based X-ray total scattering data were collected using an X-ray energy of 58.6491 keV (λ = 0.2114 Å) at beamline 11-ID-B of the Advanced Photon Source (APS), Argonne National Laboratory (APS). The measurement was performed using the rapid acquisition PDF method by employing a

Perkin Elmer amorphous silicon detector. The image plate was exposed for 1.2 s and the measurement was repeated 75 times for a total collection time of 90 s for each sample. The software Fit2D was used to integrate and convert the 2-D raw data to 1-D intensity versus wave vector (Q) data. The PDF, G(r), was obtained from the raw 1-D data using the program PDFgetX2.

RESULTS AND DISCUSSION

During the synthesis of δ-MnO_2, the amount of added MnO_4^- was in excess relative to the stoichiometric ratio of Mn(II), as shown in equation 1.

$$2MnO_4^- + 3Mn^{2+} + 2H_2O \rightarrow 5\delta\text{-}MnO_2 + 4H^+ \quad (1)$$

Therefore, the supernatant color changed to purple after the two solutions were mixed. After the solution was heated to 100 °C for 14 min, the color of the supernatant changed from purple to colorless owing to the complete reduction of the MnO_4^- ions in the presence of acidic conditions (pH = 0.86) according to equation 2.[22, 28]

$$4MnO_4^- + 4H^+ \rightarrow 4\delta\text{-}MnO_2 + 3O_2 + 2H_2O \quad (2)$$

Morphological evolution. HRTEM, FESEM, and electron diffraction were used to elucidate the kinetics of the morphological evolution during the phase transformation. After $NaMnO_4$ and $MnSO_4$ were mixed, a three-dimensional morphology of aggregation of approximately 100 nm in width was observed (Figure S2A), and primary nanoflakes were observed using HRTEM after ultrasonic dispersion (Figures 1A, B). This indicates that the primary nanoflakes aggregated loosely driven by the surface energy. The edges of the primary nanoflakes were approximately 3 to 4 nm (Figure 1B and S4). The lattice cannot be observed in Figure 1B owing to the poor crystallinity of the nanoflakes. Furthermore, the selected area diffraction (SAED) (inset of Figure 1B) shows two diffuse diffraction rings at ~0.24 nm and ~0.14 nm, which is consistent with the $d_{(100)}$ = 0.24 nm and $d_{(110)}$ = 0.14 nm spacings of δ-MnO_2, respectively. Additionally, the absence of the (001) and (002) diffraction rings in the SAED indicate that at this stage the poor crystallization of the nanoflakes consist of no more than a few [MnO_6] octahedral layers. The atomic force microscopy (AFM) results in Figure 1C show two-dimensional

nanoflakes with an average height of approximately 0.35 nm (Figure 1D), which is consistent with the thickness of a single [MnO_6] octahedral layer.

When the suspension is heated for 6 min, nanoribbons appear (with lengths ranging from 20 to 60 nm and widths from 3 to 7 nm, as shown in Figures 2A, B). In addition, the nanoribbon is aggregated from many nanoflakes in Figures 2B, C. A diffraction ring is also observed in the SAED pattern at ~0.14 nm and ~0.24 nm and originates from the (110) and (100) reflections of δ-MnO_2 (inset of Figure 2B). Although the morphology changes, no other diffraction peaks appear. The thickness of the nanoribbon in Figure 2C is only 0.356 nm that confirms that the nanoribbons maintain a single-layer δ-MnO_2 structure. The assembly of δ-MnO_2 at low pH is energetically favored because the primary nanoflakes have high-surface energy, low-Na^+ content, and hydroxyls on edge sites which can generate hydrogen bonding with the adjacent nanoflakes.[4]

When the suspension is heated for 10 min, the width and length of the nanoribbons increase to ~30 nm and ~100 nm, respectively (Figure 3A). HRTEM images show in the sectioning of the nanosheets along the (001) plane in Figure 3B reveal that nanoribbons are thickened by the assembly and form nanorods with a thickness of ~7 nm (the sectioning schematic along the (001) plane is shown in Figure S3A). The measured d_{hkl} spacing of 0.69 nm corresponds to the (110) plane of α-MnO_2 in Figure 3D. The observed nanorods exhibit different sizes and crystallographic orientations owing to the assembly of the multiple primary nanorods (Figure 3B). The nanoribbons are cut off along the [110] direction (as shown in Figure 3C, and the cutting schematic along the (001) plane is shown in Figure S3B). It is shown that the length of the nanoribbons is ~40 nm. However, the observed thickness of the nanoribbons (2.24 nm) corresponds to only three [MnO_6] octahedral layers. The top [MnO_6] octahedral layer assembled on the nanosheet has a d spacing of 1.00 nm, which is larger than the $d_{(110)}$ value of the lower layer (Figure 3C). Furthermore, the size of this layer shown in blue squares in Figure 3C is 6.7 nm, which corresponds to the typical lateral dimensions of the nanoflakes, and indicates that the nanoribbons thicken by the face-to-face assembling of the nanoflakes. The AFM image in Figure S5B also reveals the assembly of the nanoflakes on the nanoribbons. The blue circles in Figures 3C mark the dislocations along the [001] and [110] directions. Because the dislocations are a common remnant of attachment events, these may indicate the

attachment of two small nanorods assembled by both end-to-end (along (001) plane) and side-to-side OA (along (110)).[20] HRTEM shows that the nanorods have serrated sides which may form during the assembly of the nanoflakes (Figure 3D).

After the suspension is heated for 14 min, large numbers of nanorods appear, coincident with the disappearance of the δ-MnO_2 nanoflakes (Figure 4A). The widths of the α-MnO_2 nanorods with better crystallinity in Figure 4B range from 8 to 10 nm. There are two nanorods that assemble at one end to form a continuous lattice along the (110) plane (Figure 4C). The number of lattice dislocations observed at the attached interface (inset I in Figure 4C) is higher than that of a single nanorod (inset II in Figure 4C). The blue square in Figure 4C indicates that two nanorods separate to form a gap at one end. This process has been extensively reported for the growth of α-MnO_2 nanorods based on the side-to-side OA process. [2, 11, 20, 29, 30]

After the final heating stage, the widths and lengths of nanorods increase to ~40 nm and ~400 nm, respectively (Figures 5A, B). The serrated sides and internal lattice dislocations of nanorods in Figure 5C have almost disappeared owing to the aging process. However, the overlap of individual sheets is still visible at the [001] ends of the rods (Figure 5C).

Structural evolution. TEM can only observe morphological changes. However, the mechanism based on which the δ-MnO_2 transformed to α-MnO_2 at 100 °C for 10 min, and the exact structural changes experienced before transformation, were studied using detailed structural characterizations. The powder XRD pattern of the initial δ-MnO_2 shows two broad diffraction peaks at 37° ($d_{(100)}$ = 2.46 Å) and 65° ($d_{(110)}$ = 1.43 Å) (Figure 6A), which can be attributed to δ-MnO_2 with poor crystallinity, small-sized and randomly stacked [MnO_6] octahedral layers, in good agreement with the SAED shown in the inset of Figure 1B.[7, 23, 31] The d-spacing ratio of $d_{(100)}$ to $d_{(110)}$ is 1.73, which indicates a hexagonal layer symmetry.[32–34] The absence of basal (001) and (002) peaks ($d_{(001)}$ = 7.2 Å , $d_{(002)}$ = 3.6 Å) is consistent with TEM and AFM images and further proves that the δ-MnO_2 possesses a single [MnO_6] octahedral layer structure (Figure 1).

Before the suspension was heated at 100 °C for 10 min, only δ-MnO_2 appeared in the XRD pattern (Figure 6A-C). The (100) and (110) diffraction peaks of δ-MnO_2 are not sharper than those for the initially formed sample, thus indicating that the sizes of the

crystallites did not increase within the a-b planes (Figure 6C).[18] A detailed inspection of these (100) and (110) peaks suggests a slight structural alteration of the δ-MnO_2 evidenced by the appearance of a small shoulder on the high angle side of the (100) peak (Figure 6C, asterisk symbol). Previous study proposed that this feature could be related to an increased amount of Mn(III) capped on vacancies in the [MnO_6] octahedral layers.[32] These results suggest that Mn(IV) is being reduced to Mn(III)/Mn(II) and adsorbed on the vacancy sites with increasing reaction times.

After the suspension is heated for 14 min, (110), (200), and (310) α-MnO_2 peaks with low intensity (ICDD No. 00–29–1020, $d_{(110)}$ = 0.69 nm, $d_{(200)}$ = 0.48 nm, and $d_{(310)}$ = 0.31 nm), thus indicating that some of the δ-MnO_2 was transformed to α-MnO_2 during heating in the time interval from 10 min to 14 min (Figure 6A).[20] The lattice spacing of 0.69 nm (Figure 3B) for the (110) plane of α-MnO_2 is observed in the XRD pattern of Na100-10 (Figure 6B). Therefore, the period along the α-MnO_2 (110) plane was formed gradually and consistent with the formation of the α-MnO_2 by the addition of the single-layer nanoflakes or the nanoribbon of the δ-MnO_2. Thickening of the nanoribbons and transformation of structures occurred simultaneously during the 10 min heating period.

Finally, the XRD half peak width narrowed and their intensities increased gradually during the heating period from 14 to 20 min. This indicated that the crystallite size and crystallinity of α-MnO_2 increased (Figure 6).

During the structural transformation, subtle changes in the XRD peak may occur owing to the reduction and migration of Mn. Therefore, we speculate that the production and adsorption of Mn(III)/Mn(II) play an important role in the transformation of δ-MnO_2 to α-MnO_2. The phenomenon based on which Mn(IV) was reduced to Mn(III)/Mn(II) and adsorbed on the vacancy sites was further confirmed by the results of the pair distribution functions (PDFs). From the peak intensity examination of PDF, a systematic structural change was observed during the synthetic process (Figure 6E). From Na100-6 to Na80, the peaks at 2.85 Å and 4.93 Å decreased in intensity. These peaks are attributed to atomic pairs involving the first and second Mn shells within the octahedral layer around specific Mn (Mn_L-Mn_L1 and Mn_L-Mn_L2) shells (Figure S6).[31, 35] By contrast, the correlations at 3.44 Å and 5.28 Å increased in intensity. These increases are attributed to the atomic pairs formed by the Mn_L and the Mn interlayer (Mn_{IL}) at vacancies belonging to the first (Mn–

$Mn_{IL}1$) and second (Mn–$Mn_{IL}2$) shells, respectively. The PDF results also suggest that Mn_L migrate from the layer to the interlayer, above or below the vacancies, to form mono-μ-oxo bridge (with an Mn_L–$Mn_{IL}1$ distance of approximately 3.44 Å) [MnO_6] octahedra.[35] It is likely that these interlayer Mn(III)/Mn(II) octahedra act as templates for the tunnel "walls" during the transformation to α-MnO_2.[11, 12]

Evolution of the chemical composition. The Mn average oxidation states (AOS) of the intermediate products further provide quantification of the Mn(III)/Mn(II) production and structural changes of the δ-MnO_2. The detailed Mn(IV), Mn(III), and Mn(II) contents, which are obtained by the fitting the XPS narrow scans of the Mn 3s spectra are listed in Table 1 and Figure S7. The AOS of the samples decreased from 3.96 to 3.70 (Table 2, titration data) during the heating period of the suspension (100 °C for 10 min). XPS Mn3s fitting data show that the percentages of Mn(IV) decreased from 92.5 % to 84.1 %, the percentage of Mn(III) increased from 6.7 % to 12 % during this stage. The values of AOS obtained by fitting of XPS $Mn2p_{3/2}$ spectra are systematically lower than those obtained by the titration method probably owing to the higher content of the lower valence Mn present at the surface.[37–39] Thus, the XPS-derived AOS represents "surface" Mn AOS, and it is possible that Mn(IV) is reduced to Mn(III)/Mn(II) and is adsorbed on the surface of the δ-MnO_2 nanoparticles. Despite the discrepancy between the absolute AOS values, we obtained similar trends in the evolution of AOS with the reaction derived from the two methods.

Previous study have shown that structural Mn(III) was critical to the transformation of layer-structured Mn oxides into tunneled ones.[40] However, the mechanism by which Mn(III) was reduced from Mn(IV) in the initial δ-MnO_2 is still an open question. As described above, some of the octahedral Mn(IV) was initially reduced to Mn(II), and part of it was subsequently transformed to Mn(III). Given that apart from O_2-H_2O (H^+) no other reductant existed during the transformation of δ-MnO_2 to α-MnO_2. There are two possible pathways to describe the reduction of Mn(IV).

One way is that the MnO_2 is reduced by H_2O at ~100 °C and pH < 1, according to the equation 3.[41]

$$MnO_2 + 2H^+ \rightarrow Mn^{2+} + H^2O + \frac{1}{2}O_2 \qquad (3)$$

Depending on the pH, the Mn(II) cations which originating from oxidation of lattice O^{2-} under acidic condition may attach above/below the layer vacancies.[11, 41, 42] The XRD pattern of the NaMix in Figure 6 shows that the crystallinity of δ-MnO_2 was poor (i.e., small crystallite size), thus indicating a large surface area, which favors equation 3.

A second possible pathway for the reduction of Mn(IV) is due to the poorly crystalline δ-MnO_2 with mixed-Mn valences (II, III, and IV) and the release of structural oxygen, according to the equation 4.[44]

$$[\text{ -Mn(IV) - } O^{2-} \text{ -Mn(IV) - }] \rightarrow [\text{ - Mn(III) - -Mn(III) - }] + \frac{1}{2}O_2 \quad (4)$$

The XPS fitting results of O1s are listed in Table 1. There are three species of oxygen in Mn oxides, including lattice oxygen (O^{2-}), hydroxide oxygen (-OH), and oxygen in molecular water. Among the three species of oxides, the O^{2-} decreased from 69.9 % to 56.2 %, and the -OH increased from 18.1 % to 26.3 % during the heating of the suspension during the first 10 min. The large amount of lost O^{2-} was not proportional to the formed -OH. It is interesting that this great loss of O^{2-} is consistent with the creation of O vacancies in the δ-MnO_2, as proposed above (equation 4). The observed increase of the O1s peak at 532.4 eV in the XPS spectra is induced by the formation of oxygen vacancies (Figure S8).[45–48] Furthermore, the increase in the content of Na^+ and Mn(III) (longer Mn-O bond), and the poor crystallinity could facilitate the formation of oxygen vacancies (Tables 1 and 2), which promote the production of Mn(III) and the transformation of a 2D layer structure into a one-dimensional (1D) tunnel structure.[41, 49, 50]

After forming the tunnel structure, the intensities of the O1s XPS peaks at 532.4 eV were maximized, and the AOS of δ-MnO_2 reached a minimum during the 10 min heating period. The reactions described in equations 3 and 4 became less favorable owing to the formation of a more stable structure of α-MnO_2, and the percentages of Mn(III) and Mn(II) which decreased gradually (Table 1). Additionally, the decrease of the O1s XPS peak at 532.4 eV was induced by the reduction of oxygen vacancies (Figure S8). This indicated that dissolved oxygen generated by the reactions of equations 3 and 4 could refill the oxygen vacancies and oxidize Mn(III)/Mn(II) back to Mn(IV) after the formation of α-MnO_2, which caused the increase of AOS from 3.70 to 3.96 (Table 2).

Coupled morphological and structural evolution. Based on the above analyses, the coupled evolutions of structure (Figure 6) and morphology (Figure S9) during the formation of α-MnO_2 are illustrated in Figure 7. Firstly, MnO_4^- is reduced by Mn(II) to produce primary nanoflakes of δ-MnO_2 with poor crystallinity and with sizes in the range of 2-4 nm. By increasing the heating time, nanoflakes aggregate serially to form nanoribbons. Secondly, the nanoribbons stack with each other to form primary nanorods, which initiate the conversion of δ-MnO_2 into α-MnO_2. Finally, the primary nanorods assemble along the (110) and (001) planes by side-to-side and end-to-end OA, respectively.

The structure of δ-MnO_2 produced in the initial crystallization stage does not meet the necessary conditions, i.e., increased proportion of Mn(III)/Mn(II) above or below the layer vacancies for its conversion to α-MnO_2. Although the δ-MnO_2 did not convert to α-MnO_2 before it was heated (for a period of 10 min), the lower pH of 0.86 was favorable for edge-to-edge aggregation along the (100) plane.[7] The initially formed nanoribbons which were formed by the nanoflakes which were attached with each other have many lattice dislocations at the grain boundaries (Figure 2B and 3C) and promote the generation of oxygen vacancies.[51] The Mn(III) moieties were generated based on the generation of oxygen.

Subsequently, structural adjustments occur through the production and migration of Mn(III) in the δ-MnO_2 nanoflakes and nanoribbons. Recently, Ling et al. showed that the amount of Mn(III) has an impact on the structure of δ-MnO_2.[52] Furthermore, Cui et al. and Yuan et al. revealed that the interlayer Mn(III) play a important role to built tunnel structure during the conversion of LMOs (buserite) to TMOs (3 × 3 todorokite).[38, 21] The amount of Mn(IV)/(III) for the ideal transition state structure can be counted as showed in Figure S10 i.e., the interlayer Mn(III) content requires 30 % of the total Mn to assemble into the α-MnO_2 structure. This agrees very well with our experimental observations. The AOS of Na100-10 and K100–4, the production of onset of transformation into α-MnO_2 was 3.70 and 3.74 with Mn(III) concentration was 30 % and 26 % of the total Mn, respectively. Sufficient Mn(III) was required for the formation of the tunnel "walls" to support the transformation, and for the provision of sufficient hydrogen bonding. Indeed, [Mn(III)O_6] octahedra are distorted by the Jahn–Teller effect, and bonding distortion within the octahedral layer is relieved when Mn(III) migrates from layers to locations above and

below the vacancies (Figure 7, step 1).[11] These [Mn(III)O_6] octahedra include three unsaturated oxygen molecules which were combined with H^+ to form -OH. When the amount of -OH was large enough, a network of hydrogen bonds formed between the [Mn(III)O_6] octahedra of adjacent nanosheets and nanoflakes (Figure 7, step 2, 3). These [Mn(III)O_6] octahedra dehydrated via a condensation reaction and formed the tunnels "walls." Therefore, the number of the -OH moieties is expected to be maximized at the initial stage of the transformation, and to decrease during the subsequent transformation stages. These nanoribbons and nanoflakes attach along the (001) plane of δ-MnO_2 to form primary α-MnO_2 nanorods based on face-to-face OA (Figure 7, step 4). This is the process of structural evolution used to promote the transformation of morphological and crystal phase changes.

To confirm this formation mechanism in the α-MnO_2 with different tunnel cations, the K^+-stabilized α-MnO_2 was synthesized with similar procedures, whereby only $NaMnO_4$ was replaced by $KMnO_4$. During the synthesis of K^+-stabilized α-MnO_2, all the trends of the structural evolution were consistent with Na^+-stabilized α-MnO_2 (Figure S11 and Table S1, S2). It is suggested that the different tunnel cations of α-MnO_2 experienced a similar OA formation process. The δ-MnO_2 molecules were converted to α-MnO_2 using heating at 100 °C for a 2 min period. The XRD analysis (Figure S11) indicate that the conversion rate of K^+-stabilized δ-MnO_2 was much faster than that of Na^+-stabilized δ-MnO_2. The structure of K^+-stabilized α-MnO_2 was stable when the suspension was aged for 24 h, while previous reports indicated that the stable (100) surface of nanorods could be formed during this stage.[20] However, when the Na^+-stabilized α-MnO_2 was continually aged for 24 h, the XRD patterns of the samples yielded a new peak d_{hkl} = 0.4 nm of γ-MnO_2 with a 1 × 2 tunnel structure (Figure S12) because of the small amount of Na^+ used (3.24 ± 0.09% in Table 2) in the tunnel to stabilize the Na^+-stabilized α-MnO_2.[50] These results indicate that the K^+ adsorbed on δ-MnO_2 not only accelerated the production and migration of Mn(III), but also promoted the structural conversion and stability of the produced α-MnO_2. This finding agrees well with previous reports that indicated that the K^+ ions whose sizes (~0.138 nm) facilitated trapping of the 2 × 2 tunnel size (~0.46 nm), played important roles in the templating and stabilization of the tunneled framework.[53]

Another difference between the K^+-stabilized α-MnO_2 and Na^+-stabilized α-MnO_2 is the dominant side crystallographic face of the products. In this study, the cutting of the nanorods of Na^+-stabilized α-MnO_2 along the (001) plane at different stages shows that the side planes of the nanorods still correspond with the (110) plane (Figure 5D, S13). This is in part attributed to the fact that the open tunnel structure is formed easier during the assembly process, and the morphology can be better captured during a slower Na synthesis. The nanorods of Na^+ stabilized α-MnO_2 with the exposed (110) lateral facets may be the intermediate products that can be stably present over a period of time due to a slow reaction rate. In the presence of K^+, the side faces of the nanorods become four (100) faces with lower energy 0.44 J/m^2 than (110) surface energy of 0.74 J/m^2 through a dissolution–recrystallization reaction (Figure S13).[19] K^+ stabilized α-MnO_2 is formed more than 5 times faster than Na^+ stabilized α-MnO_2 during the same synthesis period, and has a longer aging time, so that the K^+ stabilized α-MnO_2 nanorods tend to expose stable (100) edge surface by the dissolution-recrystallization driven by the surface energy difference. Therefore, α-MnO_2 nanorods with different exposed lattice faces can be controlled during the synthesis according to the specific application. The Na^+-stabilized α-MnO_2 is more suitable for producing nanorods with four (110) lateral faces, which likely reduce the distance and energy barrier for ion diffusion, and improve the rate performance of α-MnO_2 in various applications, such as rechargeable battery electrodes, supercapacitors, and Li-O_2 battery catalysts.[17, 54–58] Conversely, the K^+-stabilized α-MnO_2 is more suitable for producing long nanowires because of its stable tunnel structure with support for K^+.

Although this study is not exhaustive, it does highlight an important area for further studies on the morphological and structural interactions. Indeed, future studies could evaluate K^+ ion template effects on the migration of Mn(III) into tunnel “walls” and the changes in the reactivities of the products which are formed in different stages.

CONCLUSION

Na^+-stabilized tunnel structured α-MnO_2 nanorods were found to assemble via the staged OA growth process. The coupling evolution of structures and morphologies during the entire process has been explored.

Firstly, the δ-MnO_2 nanoflakes, which possessed poorly crystalline forms, aggregated along the (110) surface plane to form δ-MnO_2 nanoribbons via the edge-to-edge aggregation mechanism. Meanwhile, the Mn(IV) ions in the [MnO_6] octahedral layer of δ-MnO_2 were reduced to Mn(III) by water, and then migrated into above and below the vacancies. Secondly, the morphology and structure of δ-MnO_2 evolved simultaneously. The Mn(III), whose amount increased gradually, built up tunnel walls and triggered the conversion of the 2D layer structure to the 1D tunnel structure. A dynamic network of hydrogen bonds between the -OH groups, which were combined with Mn(III) of adjacent nanoribbons, were present as a mode of bonding to fabricate the tunnel structure. Therefore, adjacent nanoribbons aggregated and formed α-MnO_2 primary nanorods based on the face-to-face OA mechanism. Thirdly, primary nanorods assembled with each other to form longer and wider nanorods based on respective end-to-end and side-to-side OA mechanisms. The defects which were formed by the assembly process were constantly smoothed via dissolution-recrystallization processes throughout the entire reaction. This work has filled the gap regarding the initial stage of 1D tunnel-structured α-MnO_2 formation in natural condition. Meanwhile, it also provided greater fundamental understanding of the relationship between the coupled structure and the morphological transformation during the crystal growth process.

ACKNOWLEDGMENT

The authors thank the National Natural Science Foundation of China (Grant Nos. 41471194 & 41171197) and the Strategic Priority Research Program of the Chinese Academy of Sciences (No. XDB15020402) for financial support of this research. Use of the Advanced Photon Source, Argonne National Laboratory, supported by U.S. DOE-BES under Contract DE-AC02-06CH11357.

REFERENCES

1. L. Penn, J. F. Banfield, *Science*, 1998, **281**, 969-971.
2. J. J. De Yoreo, P. U. Gilbert, N. A. Sommerdijk, R. L. Penn, S. Whitelam, D. Joester, H. Zhang, J. D. Rimer, A. Navrotsky, J. F. Banfield, *Science*, 2015, **349**, aaa6760.
3. J. Zhang, F. Huang, Z. Lin, *Nanoscale*, 2010, **2**, 18-34.
4. X. Liang, Z. Zhao, M. Zhu, F. Liu, L. Wang, H. Yin, G. Qiu, F. Cao, X. Liu, X. Feng, *Environ. Sci.: Nano*, 2017, **4**, 1656-1669.

5. H. Zhao, M. Zhu, W. Li, E. J. Elzinga, M. Villalobos, F. Liu, J. Zhang, X. Feng, D. L. Sparks, *Environ. Sci. Technol*, 2016, **50**, 1750-1758.
6. W. Qian, X. Liao, W. Xu, R. Yang, K. J. Livi, M. Zhu, *Inorg. Chem*, 2016, **55**, 10248-10258.
7. F. F. Marafatto, B. Lanson, J. Peña, *Environ. Sci.: Nano*, 2018, **5**, 497-508.
8. A. L. Atkins, S. Shaw, C. L.Peacock, *Geochim Cosmochim Ac*, 2014, **144**, 109-125.
9. S. L. Suib, *Accounts Chem Res*, 2008, **41**, 479-487.
10. S. Dharmarathna, C. K. King'Ondu, W. Pedrick, L. Pahalagedara, S. L. Suib, *Chem Mater*, 2012, **24**, 705–712.
11. S. Grangeon, A. Fernandezmartinez, F. Warmont, A. Gloter, N. Marty, A. Poulain, B. Lanson, *Geochem T*, 2015, **16**, 12.
12. S. Grangeon, B. Lanson, M. Lanson, *Acta Crystallogr B Struct Sci Cryst Eng Mater*, 2014, **70**, 828-838.
13. Y. F. Yuan, C. Liu, B. W. Byles, W. Yao, B. Song, M. Cheng, Z. Huang, K. Amine, E. Pomerantseva, R. Shahbazian-Yassar, J. Lu, *Joule*, 2019, **3**, 1-14.
14. J. Liu, V. Makwana, J. Cai, S. L. Suib, M. Aindow, *J. Phys. Chem. B*, 2003, **107**, 9185-9194.
15. S. Parc, D. Nahon, Y. Tardy, P. Bieillard, *Am. Mineral*, 1989, **74**, 466-475.
16. J. Ostwald, *Econ. Geol*, 1992, **87**, 1237-1252.
17. P. M. Vasconcelos, P. R. Renne, G. H. Brimhall, T. A. Becker. *Geochim. Cosmochim. Aacta*, 1994, **58**, 1635-1665.
18. T. T. Truong, Y. Liu, Y. Ren, L. Trahey, Y. Sun, *Acs Nano*, 2012, **6**, 8067-8077.
19. K. Li, J. Chen, Y. Peng, W. Lin, T. Yan, J. Li, *J. Mater. Chem. A*, 2017, **5**, 20911-20921.
20. Y. Yuan, S. M. Wood, K. He, W. Yao, D. Tompsett, J. Lu, A. Nie, M. S. Islam, S. Santhanagopalan, *Acs Nano*, 2016, **10**, 539–548.
21. Y. F. Yuan, K. He, B. W. Byles, C. Liu, K. Amine, J. Lu, E. Pomerantseva, R. Shahbazian-Yassar, *Chem*, 2019, **5**, 1793-1805.
22. S. Grangeon, B. Lanson, M. Lanson, *Acta Crystallogr. B*, 2014, **70**, 828–838.
23. D. Portehault, S. Cassaignon, E. Baudrin, J. P. Jolivet, *J. Mater. Chem*, 2009, **19**, 2407-2416.
24. D. Portehault, S. Cassaignon, E. Baudrin, J. Jolivet, *Chem Mater*, 2007, **19**, 5410-5417.
25. D. Zhai, B. Li, C. Xu, H. Du, Y. He, C. Wei, F. Kang, *J. Power. Sources*, 2011**, 196**, 7860-7867.
26. N. Kijima, H. Yasuda, T. Sato, Y. Yoshimura, *J. Solid. State Chem*, 2001, **159**, 94-102.
27. E. S. Iton, J. E. Post, P. J. Heavey, F. T. Ling, S. N. Kerisit, *Appl. Surf. Sci*, 2016, **366**, 475-485
28. R. M. Mckenzie, *Mineral Mag*, 1971, **38**, 493-502.
29. H. Zhang, J. J. De Yoreo, J. F. Banfield, *Acs Nano*, 2014, **8**, 6526-6530.
30. X. Zhang, Y. He, M. L. Sushko, J. Liu, L. Luo, J. J. De Yoreo, S. X. Mao, C. M. Wang, K. M. Rosso, *Science*, 2017, **356**, 434-437.
31. M. Villalobos, B. Toner, J. Bargar, G. Sposito, *Geochim. Cosmochim. Ac*, 2003, **67**, 2649-2662.
32. V. A. Drits, B. Lanson, A. C. Gaillot, *Am Mineral*, 2007, **92**, 771-788.
33. S. Grangeon, B. Lanson, N. Miyata, Y. Tani, A. Manceau, *Am Mineral*, 2010, **95**,

1608-1616.
34. H. Yin, W. Tan, L. Zheng, H. Cui, G. Qiu, F. Liu, X. Feng, *Geochim. Cosmochim. Ac*, 2012, **93**, 47-62.
35. A. Manceau, M. A. Marcus, S. Grangeon, M. Lanson, B. Lanson, A. C. Gaillot, S. Skanthakumar, L. Soderholm, *J. Appl. Crystallogr*, 2013, **46**, 193–209.
36. V. Petkov, Y. Ren, I. Saratovsky, P. Pastén, S. J. Gurr, M. A. Hayward, K. R. Poeppelmeier, J. F. Gaillard, *Acs Nano*, 2009, **3**, 441-5.
37. I. Zaharieva, P. Chernev, M. Risch, K. Klingan, M. Kohlhoff, A. Fischer, H. Dau, *Energ. Environ. Sci*, 2012, **5**, 7081-7089.
38. H. Yin, F. Liu, X. Feng, T. Hu, L. Zheng, G. Qiu, L. K. Koopal, W. Tan, *Geochim. Cosmochim. Ac*, 2013, **117**, 1-15.
39. H. Yin, X. Feng, G. Qiu, W. Tan, F. Liu, *J. Hazard. Mater*, 2011, **188**, 341-349.
40. H. Cui, X. Liu, W. Tan, X. Feng, F. Liu, H. Daniel Ruan, *Clays. Clay. Miner*, 2008, **56**, 397-403.
41. A. T. Stone, *Environ. Sci. Technol*, 1987, **2**, 979-988.
42. E. B. Godunov, A. D. Izotov, I. G. Gorichev, *Inorg Mater*, 2018, **54**, 66-71.
43. E. B. Godunov, I. V. Artamonova, I. G. Gorichev, Y. A. Lainer, *Russian Metallurgy*, 2012, **1**, 39-44.
44. J. Hou, Y. Li, L. Liu, L. Ren, X. Zhao, *J. Mater. Chem. A*, 2013, **1**, 6736-6741.
45. M. Xing, J. Zhang, F. Chen, B. Tian, *Chem Commun (Camb)*, 2011, **47**, 4947-4949.
46. K. Wang, Y. Chang, L. Lv, Y. Long, *Appl. Surf. Sci*, 2015, **351**, 164-168.
47. Y. Sun, X. Yan, X. Zheng, Y. Liu, Y. Shen, Y. Zhang, *Nano Res*, 2016, **9**, 1116-1124.
48. J. P. Holgado, G. Munuera, J. P. Espinós, A. R. González-Elipe, *Appl. Surf. Sci*, 2000, **158**, 164-171.
49. X. Li, J. Ma, L. Yang, G. He, C. Zhang, R. Zhang, H. He, *Environ Sci Technol*, 2018, **52**, 12685-12696.
50. G. Zhang, W. Dong, X. Huang, J. Zou, *Catal Commun*, 2017, **89**, 117-120.
51. J. A. Dawson, I. Tanaka, *ACS Appl. Mater. Interfaces*, 2014, **6**, 17776-17784
52. F. T. Ling, J. E. Post, P. J. Heaney, E. S. Ilton, *Chem Geol*, 2018, **479**, 216-227.
53. J. A. Dawson, I. Tanaka, *Acs. Appl. Mater. Inter*, 2014, **6**, 17776-17784.
54. C. Wei, C. Xu, B. Li, H. Du, D. Nan, F. Kang, *J. Power. Sources*, 2013, **225**, 226-230.
55. L. Li, C. Nan, J. Lu, Q. Peng, Y. Li, *Chem Commun*, 2012, **48**, 6945-6947.
56. T. S. Arthur, R. Zhang, L. Chen, P. A. Glans, X. Fan, J. Guo, F. Mizuno, *Acs. Appl. Mater. Inter*, 2014, **6**, 7004-7008.
57. G. S. Hutchings, J. Rosen, D. Smiley, G. R. Goward, P. G. Bruce, F. Jiao, *J. Phys. Chem. C*, 2014, **118**, 12617-12624.
58. Y. Qin, J. Lu, P. Du, Z. Chen, Y. Ren, T. Wu, J. T. Miller, J. Wen, D. J. Miller, Z. Zhang, *Energ. Environ. Sci*, 2013, **6**, 519-531.
59. W. Xiao, H. Xia, J. Y. H. Fuh, L. Lu, *J. Power. Sources*, 2009, **193**, 935-938.

Table 1. Compositions of Mn and O species derived from fittings of Mn (3s) and O (1s).

Samples	Mn			O		
	Mn(III) (±0.003)	Mn(II) (±0.001)	Mn(IV) (±0.003)	O^{2-}	OH^-	H_2O
NaMix	0.067	0.008	0.925	0.699	0.181	0.120
Na100-4	0.100	0.001	0.889	0.621	0.224	0.155
Na100-10	0.120	0.039	0.841	0.562	0.263	0.175
Na100-14	0.091	0.029	0.880	0.610	0.229	0.161
Na80	0.048	0.00	0.931	0.685	0.192	0.123

Table 2. Na^+ content, average oxidation states (AOS) of Mn in intermediate products at various time intervals during Na^+-stabilized α-MnO_2 formation obtained from titration and fittings of Mn $2p_{3/2}$ and Mn 3s

Samples	XPS (Mn $2p_{3/2}$)	XPS(Mn 3s)	Titration	Chemical Composition
NaMix	3.81	3.92	3.96 ± 0.01	$Na_{0.029}MnO_{1.994}\square 0.54H_2O$
Na100-0	-	-	3.96 ± 0.02	$Na_{0.039}MnO_{1.999}\square 0.63H_2O$
Na100-4	3.78	3.87	3.86 ± 0.02	$Na_{0.055}MnO_{1.957}\square 0.77H_2O$
Na100-6	-	-	3.75 ± 0.03	-
Na100-10	3.76	3.79	3.70 ± 0.01	$Na_{0.090}MnO_{1.895}\square 0.86H_2O$
Na100-14	3.78	3.85	3.78 ± 0.04	$Na_{0.067}MnO_{1.923}\square 0.57H_2O$
Na100-16	-	-	3.95 ±0.02	$Na_{0.061}MnO_{2.006}\square 0.67H_2O$
Na100-18	-	-	3.98 ± 0.03	$Na_{0.057}MnO_{2.018}\square 0.62H_2O$
Na100-20	-	-	3.96 ± 0.01	$Na_{0.048}MnO_{2.004}\square 0.53H_2O$
Na80	3.83	3.91	3.92 ± 0.02	$Na_{0.032}MnO_{1.976}\square 0.67H_2O$

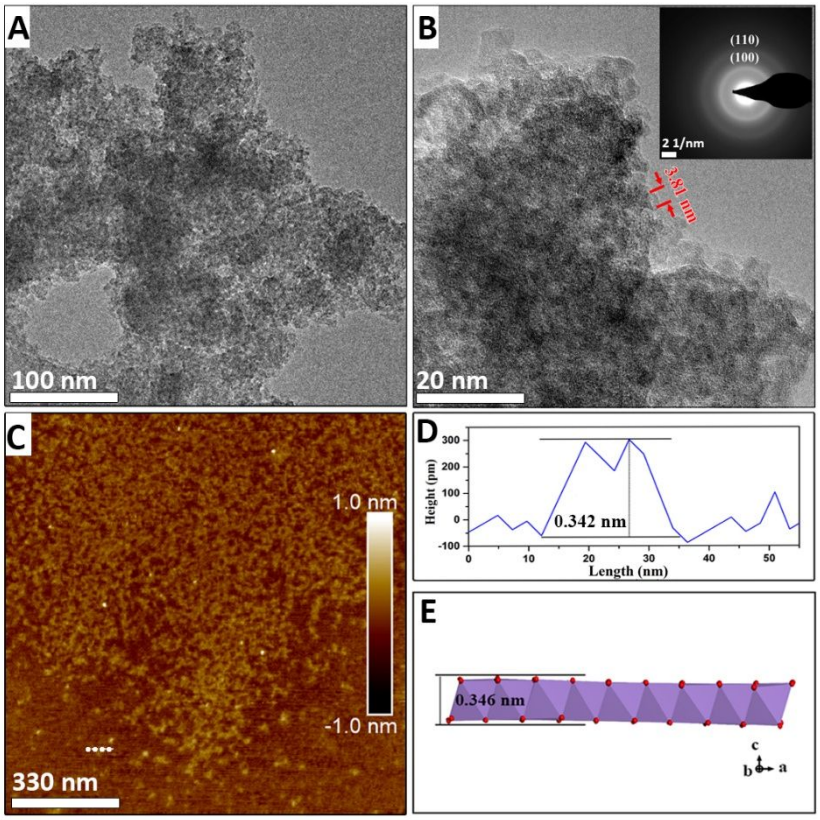

Figure 1. TEM images of intermediate product of NaMix (a, b) and the SAED pattern (b inset) recorded by focusing the electron beam in the area of image b. AFM image (c) of the intermediate product of NaMix. Profiles image (d) correspond to the trajectories shown in Figure 1c. (e) schematic of single layer δ-MnO_2.

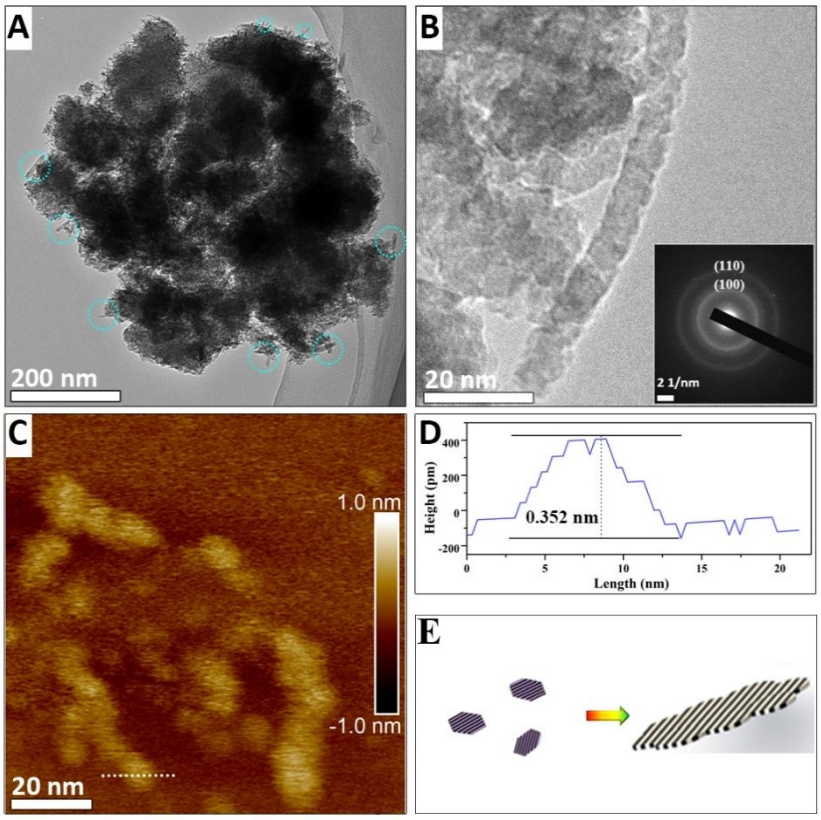

Figure 2. TEM images of intermediate product of Na100-6 (A, B) and the SAED pattern (B inset) recorded by focusing the electron beam of image b. The blue circle in image (A) indicates there are some nanoribbons. AFM image of the intermediate product of Na100-6 (C) and height profile of the Na100-6. Profiles image (D) corresponds to the trajectories shown in Figure 2c. (E) Schematic of δ-MnO_2 assembly process.

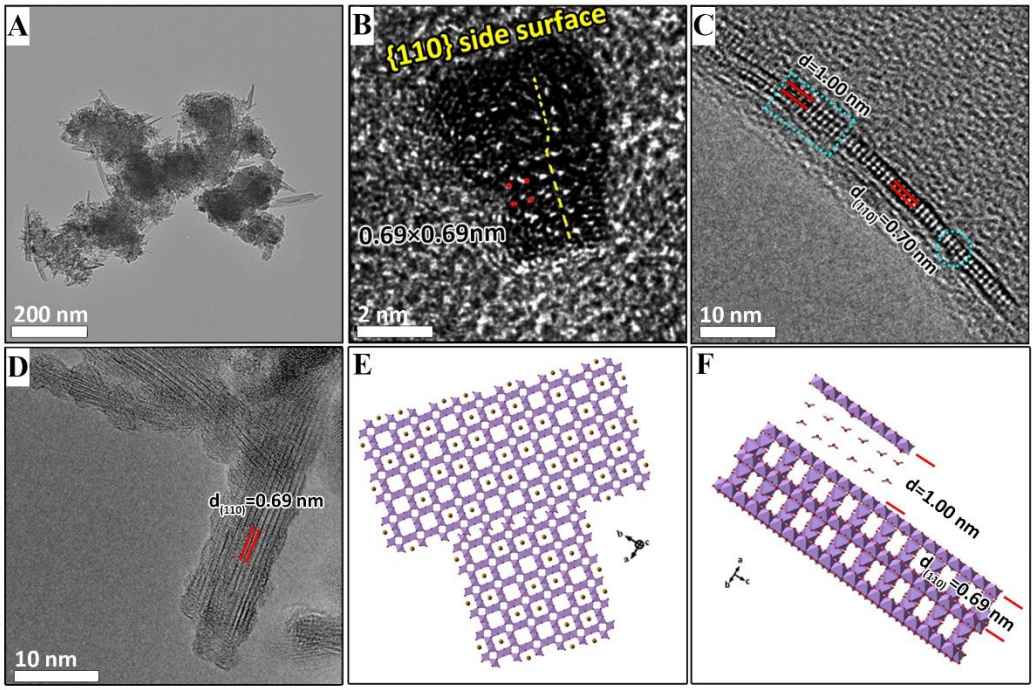

Figure 3. TEM (A) images of the intermediate Na100–10. (B) High-resolution transmission electron microscopy (HRTEM) image of a primary α-MnO_2 nanorod cross-section viewed along the [001] zone axis. (C) HRTEM image of the δ-MnO_2 nanoribbon cross-section view along the [110] zone axis. The blue circle indicates nanoflakes assembled along the (100) plane. (D) HRTEM image of nanorods. (E–F) Schematics of HRTEM images in (B) and (C), respectively.

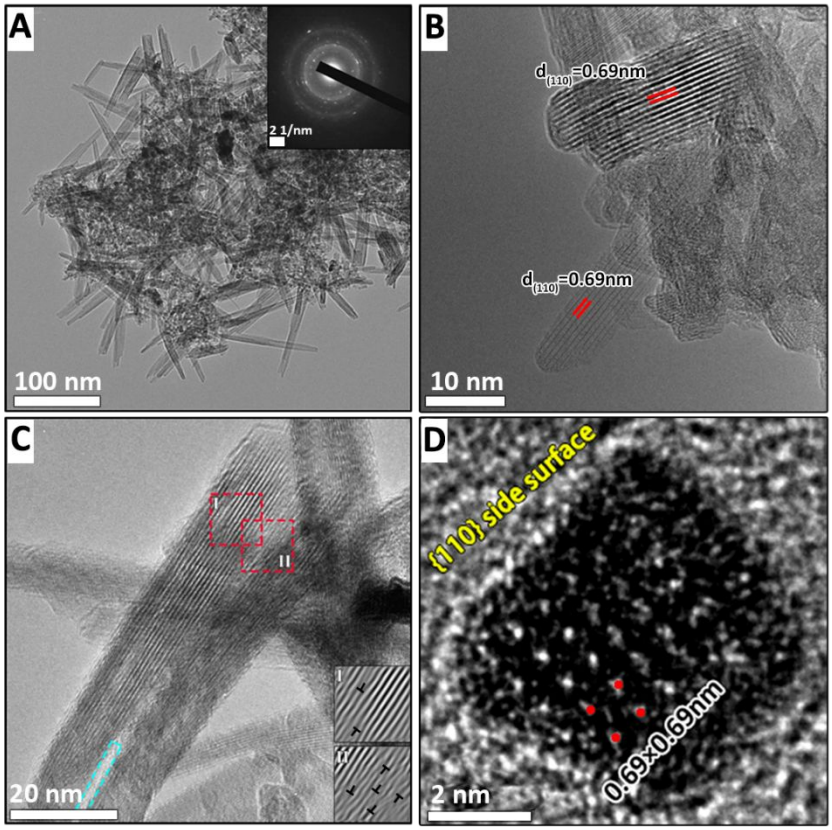

Figure 4. TEM (A) images of the intermediate Na100-14. (B) An HRTEM image of nanorods. (C) HRTEM images show nanorods assemble along (110) plane. The blue rectangle indicates that there is a gap between two nanorods. Fourier filtered images of zone I and zone II using red area outlined in (C), highlighting the defects. (D) An image of a nanorod cross section viewed along the [001] zone axis.

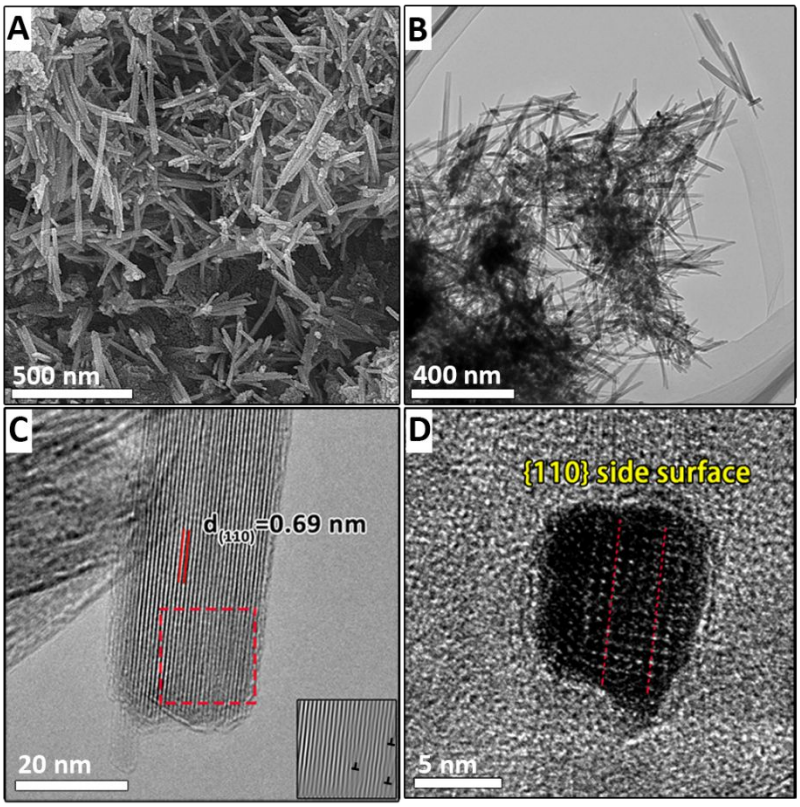

Figure 5. FESEM image of product of Na80 (A), TEM image (B) and HRTEM image (C) showing α-MnO_2 nanoparticles. Fourier filtered image (c inset) using red area outlined in (C), highlighting the defects. (D) An image of a nanorod cross section viewed along the [001] zone axis

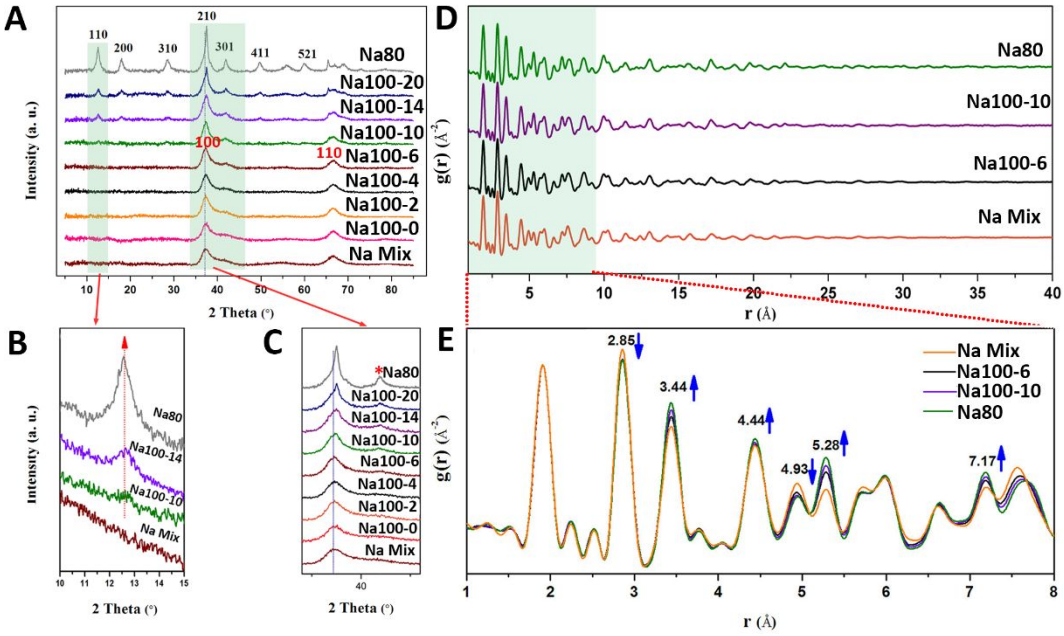

Figure 6. (A) X-ray diffraction (XRD) patterns of intermediate products at different intervals of Na^+ stabilized α-MnO_2 formation and crystal growth. Red indicates the crystal surface of the δ-MnO_2, black indicates the crystal surface of α-MnO_2 (B, C). The green zone is shown in a magnified view. The asterisk in (C) is a sign of shoulder peaks. (E, D) Pair distribution functions [G(r)s] of intermediate products at different time intervals of Na^+ stabilized α-MnO_2 formation and crystal growth.

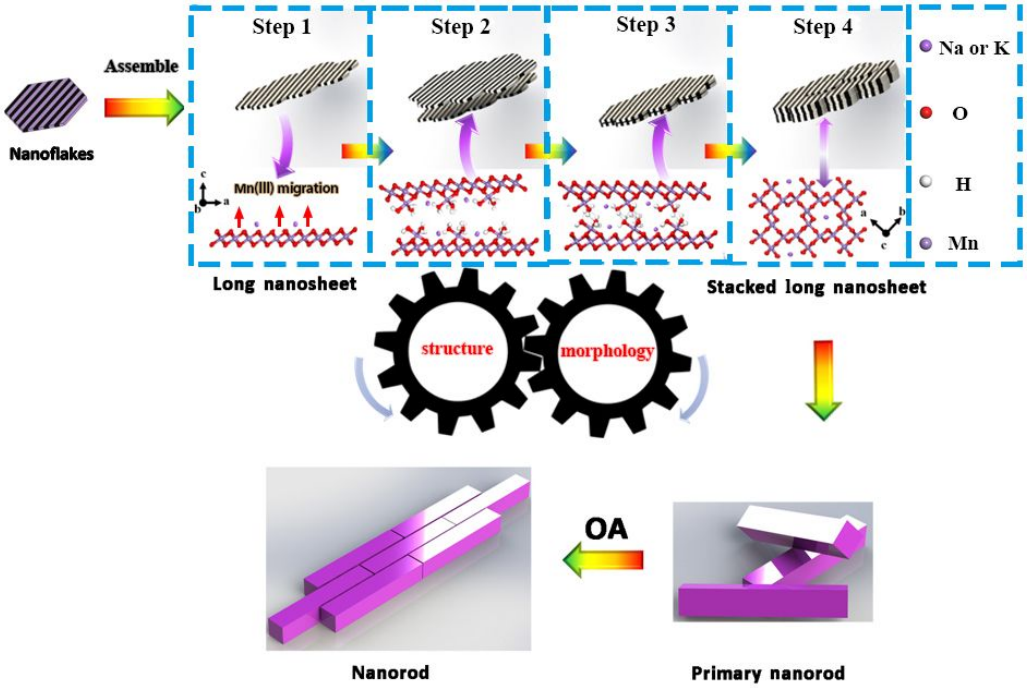

Figure 7. Proposed processes of assembly of nanoparticles and morphological evolution with time during the crystal growth of α-MnO_2 via a staged OA process. The schematic in the blue square illustrates the structural changes and morphological evolutions during the δ-MnO_2 transform to α-MnO_2.